

Suppression of the parasitic buffer layer conductance in InSb/Al_xIn_{1-x}Sb heterostructures using a wide-band-gap barrier layer

A. M. Gilbertson,¹ P. D. Buckle,² M. T. Emeny,³ T. Ashley,³ and L. F. Cohen¹

¹*Blackett Laboratory, Imperial College London, Prince Consort Road, London, SW7 2BZ, United Kingdom*

²*Department of Physics and Astronomy, The Parade, Cardiff University, Cardiff, CF24 CAA, United Kingdom*

³*QinetiQ, Saint Andrews Road, Malvern, Worcestershire, WR14 3PS, United Kingdom*

(Received 25 May 2011; published 12 August 2011)

InSb/Al_xIn_{1-x}Sb heterostructures display intrinsic parallel conduction in the buffer layer at room temperature that limits exploitation of the high-mobility two-dimensional electron gas (2DEG), particularly for nanostructured devices where deep isolation etch processing is impractical. Here, we demonstrate a strategy to reduce the parasitic conduction by the insertion of a pseudomorphic barrier layer of wide-band-gap alloy below the QW. We have studied the high-field magnetotransport in two types of InSb/Al_xIn_{1-x}Sb modulation doped quantum well heterostructures with and without the barrier layer in the temperature range 2–290 K and magnetic fields to 7.5 T. The conduction in the doping layer, the 2DEG, and the buffer layer are analyzed using a multi-carrier model that successfully captures the field dependence of the Hall resistance over the experimental field range. Samples with the barrier layer show significantly reduced buffer layer conduction compared to samples without. Our results are expected to be of importance for ambient temperature nano-electronic operation.

DOI: [10.1103/PhysRevB.84.075474](https://doi.org/10.1103/PhysRevB.84.075474)

PACS number(s): 73.63.Hs, 72.20.My, 72.80.Ey

I. INTRODUCTION

There is currently great interest in materials with enhanced electronic properties at room temperature (RT) due to their importance for applications, such as low-power, high-speed logic devices,^{1–3} magnetic storage^{4,5} and magnetic detection.⁶ The technological demands for device miniaturization and nanoscale dimensions in such applications have been well enumerated. The two-dimensional electron gases (2DEGs) formed in narrow band-gap III-V semiconductors offer the largest mobilities and saturation velocities at RT owing to a light effective mass. Electron mobilities of 4 m²/Vs are routinely obtained in modulation doped InSb/Al_xIn_{1-x}Sb quantum well (QW) structures,^{7,8} with a highest value of 6 m²/Vs reported in 30-nm-wide InSb QWs.⁹ State-of-the-art *n* and *p*-type InSb QW-field effect transistors (FETs) with sub-100-nm gate lengths have been demonstrated with record *f*_T cutoff frequencies as a result.^{1,2} Concomitant with a high mobility is a long momentum mean free path ($l_0 = \hbar k_F \mu / e$, where k_F is the Fermi wave vector), offering the potential to exploit mesoscopic effects at RT. For example, the magnetoresistance (MR) response of ballistic four-terminal junctions is particularly attractive for the detection of small magnetic fields with high sensitivity and spatial resolution.^{10,11} These studies were performed at low temperatures where the large mean free path makes the ballistic regime readily accessible. However, even at 300 K, the mean free path in InSb (and InAs) 2DEGs is on the order of 500 nm, in principle permitting transport in nanoscale devices to be almost fully ballistic. The application of ballistic devices operating at room temperature would not be limited to magnetic detection, but may pave a way to explore numerous concepts previously restricted to low temperatures (e.g. ballistic rectifiers,¹² photovoltaic devices,¹³ and ratchets¹⁴).

Reports of ballistic transport in mesoscopic InSb/Al_xIn_{1-x}Sb devices have, however, been limited to $T \leq 205$ K due to poor electrical isolation of the 2DEG rather than size arguments.¹⁵ Quasi-1D narrow channels are typically

formed by shallow mesa-etching^{15,16} or surface gates^{17,18} to confine the 2DEG. Both techniques have proved successful for InSb/Al_xIn_{1-x}Sb structures at low temperatures, but unacceptable gate leakage prohibits the use of the latter at temperatures much greater than 10 K.¹⁷ For shallow mesa-etched channels, the surrounding Al_xIn_{1-x}Sb buffer layer becomes electrically significant at temperatures > 150 K, and the parallel conduction reduces the measured ballistic component from the 2DEG to the extent where it is no longer well defined. Here, the problem lies in the thick buffer layers used for the growth of InSb/Al_xIn_{1-x}Sb heterostructures onto GaAs substrates that make a full isolation etch impractical for mesoscopic device structures. We emphasize that this volume-enhanced parallel conduction is not encountered in wide channels fabricated using conventional deep mesa etching, but is a feature of shallow etching. Furthermore, it is a mechanism that, in principle, can be suppressed by improved metamorphic buffer layer technology to reduce the total thickness or, by alternative layer designs, to reduce the buffer layer leakage, as is investigated here.

In this paper, we show that the parasitic buffer layer conduction in InSb/Al_xIn_{1-x}Sb heterostructures at room temperature can be substantially reduced by insertion of a barrier layer beneath the QW made from a thin pseudomorphic layer of wider-band-gap alloy. In this way we are able to prohibit the leakage current into the bulk of the buffer layer without compromising the 2DEG mobility. We describe high-field magnetotransport measurements on two sets of InSb/Al_xIn_{1-x}Sb QW heterostructures with and without a 15 nm Al_{0.3}In_{0.7}Sb barrier layer below the QW. These samples exhibit varying degrees of parallel conduction in the temperature range 2–290 K. The conduction in the different regions of the heterostructure is analyzed using a multi-carrier model which provides an accurate description of ρ_{xy} over the entire experimental field range. The impact of the measured material properties on the transport in realistic mesa-etched mesoscopic devices is discussed. In particular, our results

indicate that the proposed buffer layer approach permits the conductance of the 2DEG to dominate at room temperature in mesa-etched nanostructures, a requirement for ballistic transport to be observed.

II. EXPERIMENTAL DETAILS

The large lattice mismatch between $\text{Al}_x\text{In}_{1-x}\text{Sb}$ and the GaAs substrate (6% for AlSb) results in a high density of misfit dislocations at the heterointerface. Transmission electron microscopy has shown that these dislocations can propagate well beyond the interface.² This structural deficiency can result in a large variation of the electrical properties in the growth direction^{19,20} and thick metamorphic $\text{Al}_x\text{In}_{1-x}\text{Sb}$ buffer layers (typically 3 μm) are commonly used to accommodate the lattice mismatch and to regain good crystallographic properties of the desired alloy. In this way, subsequent growth of InSb QWs with high mobilities is achieved with remote delta doping (in the range 10–40 m^2/Vs at 2 K and 4–6 m^2/Vs at 300 K).^{8,9,21,22}

Here, we study the electronic properties of two sets of modulation doped InSb/ $\text{Al}_x\text{In}_{1-x}\text{Sb}$ QW heterostructures grown by molecular beam epitaxy onto semi-insulating GaAs (100) substrates. The layer structure of the samples and a Poisson solution for the energy band profile are shown in Figs. 1 and 2, respectively. Growth of the samples was initialized with a GaAs (200 nm)/AlSb (200 nm) nucleation layer. The samples are distinguished by their subsequent buffer layer schemes. The first series of samples were grown with a 3- μm -thick $\text{Al}_{0.15}\text{In}_{0.85}\text{Sb}$ layer, which we refer to as a standard buffer layer (SBL) and are labeled accordingly as SBL-1 and SBL-2. Samples SBL-1 and SBL-2 have two Te δ -layers in the $\text{Al}_{0.2}\text{In}_{0.8}\text{Sb}$ cap with a 25 nm and 15 nm relative separation, respectively [see Fig. 1(a)]. The doping density is nominally identical in both SBL samples. The second series of samples were grown with a modified buffer layer (MBL) referred to as MBL-1 and MBL-2. These latter samples have a 15-nm-thick pseudomorphic $\text{Al}_{0.3}\text{In}_{0.7}\text{Sb}$ layer inserted 300 nm beneath the InSb QW. The purpose of this layer is to provide a barrier such that electrons and holes thermally generated in the underlying 2.7- μm $\text{Al}_{0.15}\text{In}_{0.85}\text{Sb}$ layer are prevented from diffusing to the Ohmic contact regions, thereby electrically isolating the majority of the buffer layer. In the MBL samples, a single Te-doped δ -layer is located in the $\text{Al}_{0.2}\text{In}_{0.8}\text{Sb}$ cap, separated from the InSb QW by a 10-nm

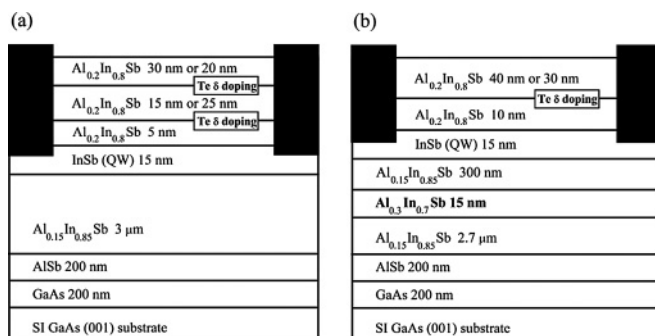


FIG. 1. (a) and (b) Layer structures of the SBL and MBL samples. Ohmic contacts are shown schematically by black boxes.

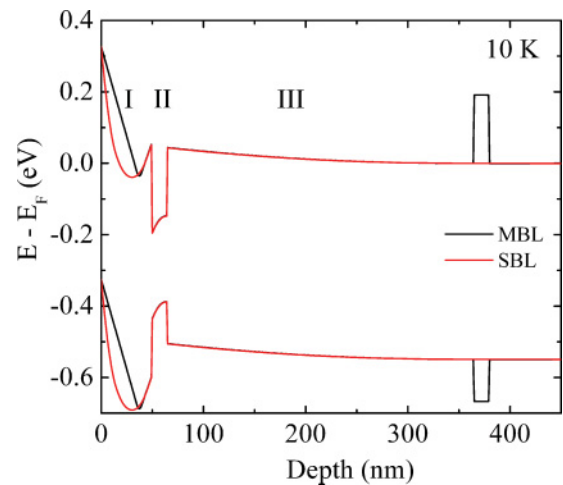


FIG. 2. (Color online) Poisson solution for the conduction and valance bands of SBL-1 and MBL-1 at 10 K. The three regions of interest are indicated; (I) the delta doped region, (II) QW, and (III) conducting buffer layer.

undoped spacer layer. The two MBL samples differ from each other only in top cap thickness and Te-doping density (fixed spacer thickness) with MBL-2 having a thinner top cap with a nominally higher doping density than MBL-1.

The conduction band offset (ΔE_c) for the $\text{Al}_x\text{In}_{1-x}\text{Sb}/\text{Al}_y\text{In}_{1-y}\text{Sb}$ interface is not well known, but assuming the relationship $0.62\Delta E_g$ found for the InSb/ $\text{Al}_x\text{In}_{1-x}\text{Sb}$ heterointerface^{23,24} is valid (a reasonable assumption since the band gap is still direct), the barrier height to electrons is of the order of 190 meV (see Fig. 2), which is significantly greater than the thermal energy ($k_B T$) at 300 K \approx 26 meV. Note that the incorporation of the barrier does not alter the conductivity of the buffer layer beneath it, but is expected to reduce the leakage current through it from the contacts.

Hall bridges 40 μm wide (with longitudinal voltage lead separation of 200 μm) were fabricated using conventional wet etching. Ohmic contacts are formed by removing the top barrier and depositing Ti/Au directly onto the exposed InSb QW (shown schematically in Fig. 1). Measurements of the Hall (R_{xy}) and longitudinal resistance (R_{xx}) were performed in the temperature range 2–290 K and in perpendicular magnetic fields up to 7.5 T using a standard low-frequency lock-in technique.

A. Multi-carrier model

In the present heterostructures, conduction may occur in the doped $\text{Al}_{0.2}\text{In}_{0.8}\text{Sb}$ top cap, the InSb 2DEG, or in the undoped $\text{Al}_{0.15}\text{In}_{0.85}\text{Sb}$ buffer layer. These correspond to the regions labelled I, II, and III in Fig. 2, respectively. At sufficiently low temperatures, the $\text{Al}_{0.15}\text{In}_{0.85}\text{Sb}$ buffer layer is depleted. However, dependent on the doping density of the δ -doped region, the $\text{Al}_{0.2}\text{In}_{0.8}\text{Sb}$ top cap layer can be occupied and even degenerate, presenting a low-mobility conducting channel in parallel to the high-mobility InSb 2DEG.²¹ At elevated temperatures, both layers can conduct, owing to thermal excitation of carriers.

In the following analysis, we consider a system consisting of three conducting layers. Due to the nature of the heterostructure, the three layers are spatially separated, but the $\text{Al}_{0.2}\text{In}_{0.8}\text{Sb}$ layer, the InSb 2DEG, and the top of the $\text{Al}_{0.15}\text{In}_{0.85}\text{Sb}$ buffer layer are in intimate contact through the shallow Ohmic contacts. The three layers can therefore be considered to experience the same local electric field, unlike an isolated layer model²⁵ (this is also reasonable due to the lateral dimensions of the device). In the case of the MBL samples, we assume that the buffer layer region beneath the $\text{Al}_{0.3}\text{In}_{0.7}\text{Sb}$ barrier is electrically isolated from the upper three layers, and contacts and can be ignored. For the cases described, the total sheet conductivity is the sum of the sheet conductivities of all contributing layers, and the conductivity tensor has the form²⁶

$$\sigma = \sum_i \begin{pmatrix} D_i & -A_i \\ A & D_i \end{pmatrix}, \quad (1)$$

where $D_i = n_i e \mu_i / [1 + (\mu_i B)^2]$, $A_i = B \mu_i D_i$, and n_i and μ_i are the sheet density and mobility of the i th layer, respectively. The sheet density of the 3D channels is related to the bulk density by $n = n_{3D} t$, where t is the layer thickness. Here, $\mu_i \geq 0$ and n_i can take positive and negative values for electrons and holes, respectively. The sheet resistivity is obtained from inverting Eq. (1). The diagonal and off-diagonal (Hall) resistivity components are related to the conductivity tensor by, respectively,

$$\rho_{xx} = \frac{\sum_i D_i}{\left[\left(\sum_i D_i \right)^2 + \left(\sum_i A_i \right)^2 \right]} \quad (2a)$$

and

$$\rho_{xy} = \frac{-\sum_i A_i}{\left[\left(\sum_i D_i \right)^2 + \left(\sum_i A_i \right)^2 \right]} = R_H B, \quad (2b)$$

where R_H is the Hall coefficient. In the low field limit ($\mu_i B \ll 1$) Eqs. (2a) and (2b) reduce to the usual expressions for multi-carrier conduction,

$$\rho_{xx} = \frac{1}{\langle n \rangle e \langle \mu \rangle} = \frac{1}{e \sum_i n_i \mu_i} \quad (3a)$$

$$R_H = \frac{1}{e \langle n \rangle} = \frac{1}{e} \frac{\sum_i n_i \mu_i^2}{\left(\sum_i n_i \mu_i \right)^2}, \quad (3b)$$

where $\langle n \rangle$ and $\langle \mu \rangle$ are the sheet density and mobility extracted from a single-carrier, single-layer analysis. Equations (2a) and (2b) exhibit a characteristic field dependence when more than one carrier is present; ρ_{xx} is constant at low fields ($\mu_i B \ll 1$), increases approximately quadratically at intermediate fields, and saturates at high field ($\mu_i B \gg 1$); ρ_{xy} is linear at low fields, distinctively sublinear at intermediate fields, and becomes linear again at high field with a Hall coefficient corresponding to the total sheet density in the system. When fitting the model to experimental data, the experimental zero field resistivity ρ_0 [Eq. (3a)] is used as a

constraint for the sum of the conductivities of the layers. In this way, the number of fitting parameters is reduced to $2i - 1$.

We would like to remark on the validity of this model to the current system under study. It is well known that bulk epitaxial InSb films exhibit a nonsaturating intrinsic MR that cannot be accounted for within a classical two-layer model.^{20,27} Various mechanisms have been proposed to describe this phenomenon, appealing to both quantum^{28,29} and classical origins, the latter typically based on mobility or density inhomogeneities in the growth direction (associated with mismatched epitaxy). A continuously varying conductivity in the growth direction cannot be captured by a discrete uniform-layer model, although the differential approach adopted by Zhang *et al.*²⁰ goes some way towards tackling the problem. For heterostructures such as those studied here, a discrete layer model is a more appropriate and accurate description because the majority of conduction occurs in the highly mobile 2DEG, but in principle, transport in the $\text{Al}_x\text{In}_{1-x}\text{Sb}$ buffer layer presents much of the same complexities as encountered in bulk InSb films. A feature of the studies^{19,20,30} to-date is that good agreement between theory and experiment for both ρ_{xx} and ρ_{xy} is rarely achieved within the same model. This is an indication that some, if not all, of the effects which manifest in ρ_{xx} and give rise to a nonsaturating MR do not enter into the Hall resistivity. This is not a new concept, e.g. weak-localization results in a negative MR with no effect on ρ_{xy} .³¹ Indeed the quantum-linear MR effect²⁹ observed in highly disordered systems, including InSb³² and graphene,³³ likewise has no effect on ρ_{xy} . Consequently, here, we fit to the experimental Hall data over the entire magnetic field range to obtain the transport properties of the layers. Furthermore, we demonstrate that a model with three layers successfully captures the full field dependence of ρ_{xy} . Consistent with earlier studies on InSb thin films,²⁰ discrepancies are found in the calculated ρ_{xx} , due to the presence of additional MR, which is not discussed here.

III. EXPERIMENTAL RESULTS

A. Low-temperature transport

Before discussing parallel conduction at elevated temperatures, which is of technological interest, we first characterize the samples by their low-temperature transport properties. Samples with the same buffer layer scheme (SBL and MBL) were found to exhibit similar high-field behavior of ρ_{xx} and ρ_{xy} at low temperatures. For brevity, we discuss data from a subset of the samples to illustrate the salient features. Figure 3 shows the high field resistivities ρ_{xx} and ρ_{xy} for SBL-1 and MBL-1 at 2 K. MBL-1 shows a single series of Shubnikov de-Haas (SdH) oscillations on a roughly constant background in ρ_{xx} and well-resolved quantum Hall plateaus in ρ_{xy} . The Hall plateaus correspond closely to the quantized values $h/e^2 \nu$ ($\nu = 1, 2, \dots$) and centered about a linear extrapolated Hall response (dashed green line). The 2D electron density of the QW is determined from the frequency of SdH oscillations to be $n_{\text{QW}} = 8.23 \times 10^{15} \text{ m}^{-2}$, which agrees with the value extracted from the low-field Hall slope ($\langle n \rangle$) to within 2%. This behavior of ρ_{xx} and ρ_{xy} indicate that only the ground state subband is occupied and that little or no parallel conduction occurs elsewhere in the heterostructure. The 2D electron mobility of the QW (μ_{QW}) is determined from ρ_0 to be $9.26 \text{ m}^2/\text{Vs}$.

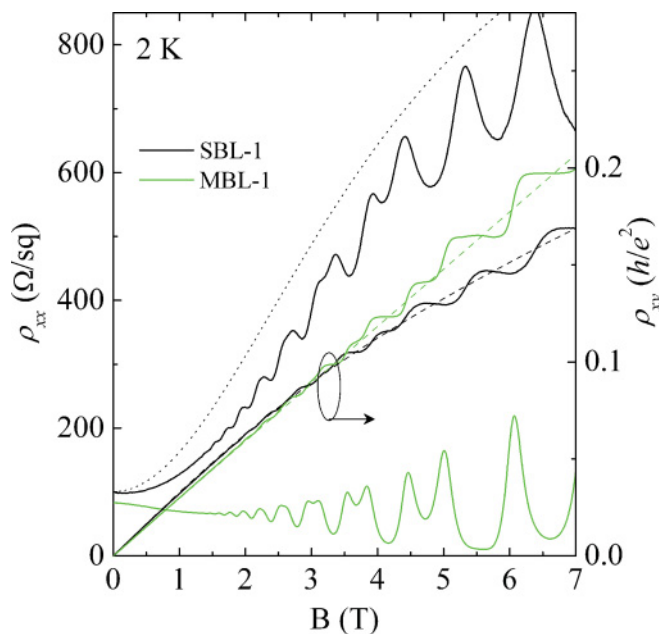


FIG. 3. (Color online) Low-temperature recordings of ρ_{xx} (left axis) and ρ_{xy} (right axis) versus magnetic field from 15-nm QW samples with SBL (SBL-1) and MBL (MBL-1). The fit to ρ_{xy} of SBL-1 with a two-carrier model is shown by the black dashed line. The black dotted line represents the calculated ρ_{xx} using the same parameters. The green dashed line shows the extrapolated linear Hall response of MBL-1.

By contrast, SBL-1 shows a single series of SdH oscillations superimposed onto an increasing non-oscillatory background MR in ρ_{xx} with a distinct sublinear Hall response in ρ_{xy} . The quantum Hall plateaus in this sample are neither flat nor equal to the quantized values. These features are symptomatic of parallel conduction in the heterostructure. In this case, one obtains from the low field (single carrier) analysis an effective carrier density ($\langle n \rangle$) and mobility ($\langle \mu \rangle$), weighted by the properties of all the conducting layers (see Sec. II A). Since at low temperatures the undoped buffer layer is depleted, we assume the parallel conduction to occur exclusively in the low mobility δ -doped $\text{Al}_{0.2}\text{In}_{0.8}\text{Sb}$ layer. Accordingly, the black dashed line in Fig. 3 shows the least squares fit of Eq. (2b) with two carriers to ρ_{xy} of SBL-1, weighted to the low field region where the quantum-oscillatory component is small. One can see that a good fit to ρ_{xy} is achieved with a two-carrier model. In the fitting procedure, we used the density of the QW $n_{\text{QW}} = 7.14 \times 10^{15} \text{ m}^{-2}$ obtained from the frequency of SdH oscillations. In this way, we obtain the parameters $n_{\delta} = 4.0 \times 10^{15} \text{ m}^{-2}$, $\mu_{\delta} = 0.16 \text{ m}^2/\text{Vs}$, and $\mu_{\text{QW}} = 8.6 \text{ m}^2/\text{Vs}$ (the subscript δ refers to the δ -doped $\text{Al}_{0.2}\text{In}_{0.8}\text{Sb}$ layer). The calculated ρ_{xx} using the same parameters (indicated by the black dotted line) deviates from the experimental data somewhat, but nevertheless reproduces, at least qualitatively, the salient features in the field dependence. We note that a good fit to ρ_{xx} with the two-carrier model could not be achieved. The discrepancy most likely originates from the existence of a weak negative MR (discussed later). The parallel channel in the SBL samples at low temperature is attributed to the

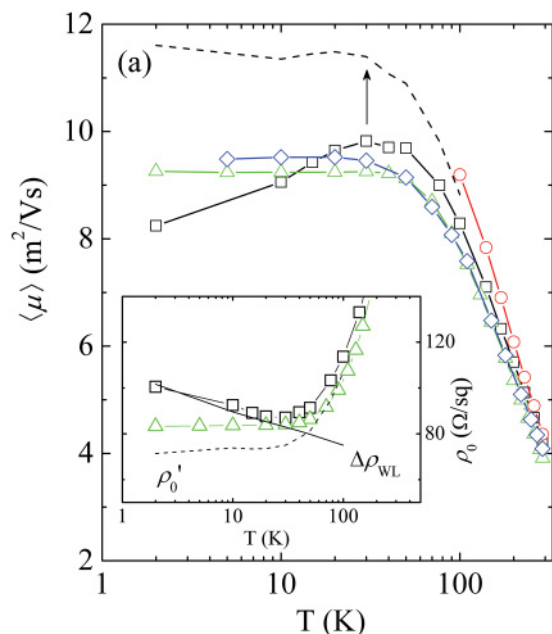


FIG. 4. (Color online) Temperature dependence of the apparent mobility $\langle \mu \rangle$ of the samples (symbols) determined from low field analysis: SBL-1 (\square); SBL-2 (\circ); MBL-1 (\triangle); MBL-2 (\diamond). The dashed line indicates the corrected mobility of SBL-1. Inset: Temperature dependence of ρ_0 for SBL-1 and MBL-1 demonstrating a logarithmic increase in ρ_0 with decreasing temperature below 40 K in the former attributed to WL. The solid line illustrates the predicted $\ln T$ dependence of $\Delta\rho_{\text{WL}}$ (plus an offset to aid comparison) and the dashed line shows the corrected ρ_0 following the method outlined in the text.

double δ -doping, which widens the conduction band minima as a function of depth in the cap layers (see Fig. 2).

In both sets of samples, $\langle n \rangle$ varies only by $\sim 10\%$ over the entire temperature range (not shown). In Fig. 4, we show the temperature dependence of $\langle \mu \rangle$ from all the samples investigated. The low-temperature mobilities of the MBL-1 and MBL-2 samples are approximately equal and remain constant up to ≈ 40 K, consistent with impurity scattering, before the onset of a strong reduction due to phonon scattering. The unusual reduction in $\langle \mu \rangle$ below 40 K observed for SBL-1 is attributed to localization effects as discussed below.

The observed reduction in $\langle \mu \rangle$ below 40 K for SBL-1 coincides with a logarithmic increase of ρ_0 [see inset to Fig. 4]. It is noteworthy that a rather weak dependence of n_{δ} and μ_{δ} on temperature is found in this range, implying that the behavior is not associated with parallel conduction. Both the $\ln T$ dependence of ρ_0 and the apparent negative MR are consistent with weak localization³⁴ (WL), which we propose is the case here. The predicted conductivity correction in 2D (for $k_F l_0 \gg 1$) takes the form of $\Delta\sigma_{\text{WL}} = -(G_0/\sigma_0)\ln(\tau_{\phi}/\tau_0)$, where $G_0 = e^2/\pi h$, $\sigma_0 = 1/\rho_0$, $\tau_0 = m^* \mu/e$ is the transport lifetime, and τ_{ϕ} is the phase coherence time.³⁵ Since $\tau_{\phi}^{-1} \propto T^p$ ($p > 0$), $\Delta\sigma_{\text{WL}}$ decays rapidly with increasing T. The mobilities $\langle \mu \rangle$ and μ_{QW} determined using ρ_0 are therefore underestimated at low temperatures. In the following we deduce a corrected mobility $\langle \mu \rangle$ by estimating $\Delta\sigma_{\text{WL}}$ to obtain the new constraint $\rho_0' = 1/(\sigma_0 - \Delta\sigma_{\text{WL}})$ in the fitting procedure. We note that the interaction effect discussed by Altshuler *et al.*³⁶ also gives

rise to a $\ln T$ conductivity correction, but in this case can be neglected due to the large Fermi energy ($E_F \propto n_{QW}$) which far exceeds the Coulomb interaction energy ($E_{e-e} \propto \sqrt{n_{QW}}$).³⁷ For the purpose of this discussion, we outline below a simple method of estimating the correction using experimental parameters. In metallic and semiconductor systems, inelastic electron-electron interactions are the dominant source of dephasing at low temperatures.^{31,38–40} In 2D systems, $\tau_\phi \propto T^{-1}$ and is well described by the Nyquist dephasing rate, given by $\tau_\phi^{-1} = (k_B T/\hbar)\pi G_0/\sigma_0 \ln(\sigma_0/2\pi G_0)$, where k_B is the Boltzmann constant.⁴¹ Substituting the experimental parameters $\sigma_0 = 10 \times 10^{-3} \Omega^{-1}$, $k_F = (2\pi\langle n \rangle)^{1/2}$, and the uncorrected $\langle \mu \rangle = 8.2 \text{ m}^2/\text{Vs}$ at 5 K, we deduce an initial value of $\Delta\sigma_{WL} = -4.1 \times 10^{-3} \Omega^{-1}$ (we used a value of $m^* = 0.03 m_0$ to calculate τ_0 , taking into account the nonparabolic conduction band from a $k.p$ approximation⁹). A value of $\rho_0' = 71.4 \Omega/\square$ was obtained by adjusting $\langle \mu \rangle$ until the difference between itself and the corrected output mobility $\langle \mu' \rangle = 1/\rho_0'\langle n \rangle e$ is equal to zero. The results of this analysis are summarized in Fig. 4. The corrected parameters obtained from fitting the two-carrier model to ρ_{xy} at 2 K using ρ_0' are $n_\delta = 3.9 \times 10^{15} \text{ m}^{-2}$, $\mu_\delta = 0.16 \text{ m}^2/\text{Vs}$, and $\mu'_{QW} = 12.2 \text{ m}^2/\text{Vs}$. This analysis results in a substantial increase in μ_{QW}' , whereas the modification to the δ -layer parameters is negligible due to their comparatively small contribution to ρ_0 (and ρ_0'). With some degree of confidence, we can therefore conclude that the low-temperature mobility of SBL-1 is greater than in MBL-1. In addition, the corrected mobility $\langle \mu' \rangle$ (dashed line) shows a similar temperature invariance below 40 K as found in the MBL samples.

The interplay between the Fermi wave vector k_F , the impurity density (n_{imp}), and screening in the scattering rates from ionized impurities and other mechanisms makes the interpretation of mobilities from different wafers difficult without the ability to modulate the 2DEG density (e.g. with a gate electrode), which we do not attempt here. Calculations of the mobility in a set of equivalent InSb/AlInSb QWs were recently performed by Orr *et al.*⁴² and Pooley *et al.*²¹ In wide 30-nm InSb QWs, typical mobilities are in the range 20–40 m^2/Vs at 2 K and found to be limited by scattering from ionized impurities in the remote δ -doped layer.^{21,42} For narrow 15-nm InSb QWs, mobilities are typically lower (7–11 m^2/Vs at 2 K), and it was found that interface roughness scattering adds a significant contribution to the total scattering rate.⁴² It follows that interface roughness scattering may also play a role in our samples. A second effect is also relevant. In heterostructures with undepleted dopant layers, the presence of electrons in the direct vicinity of the ionized impurities can enhance the mobility by additional screening of the potential fluctuations felt by the 2DEG. Given the residing electron density in the δ -doped $\text{Al}_{0.2}\text{In}_{0.8}\text{Sb}$ layer of the SBL samples, we suggest that self-screening contributes to the measured large mobility. This effect was also found relevant in 30-nm InSb/AlInSb QWs with parallel conduction in the δ -doped layer.⁴³

B. Transport at elevated temperatures

In this section, we assess the degree of parallel conduction in the samples with different buffer layer schemes at elevated

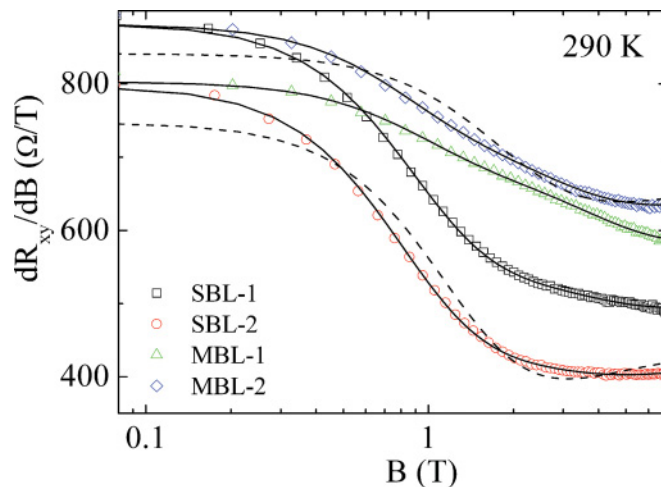


FIG. 5. (Color online) Field dependence of the Hall coefficient for the samples at 290 K (symbols); SBL-1 (\square), SBL-2 (\circ), MBL-1 (\triangle), MBL-2 (\diamond). The solid lines show fits with a three-carrier model, and the dashed line shows fits with a two-carrier model.

temperatures with particular emphasis on conduction in the buffer layer. Parallel conduction in the SBL samples occurs over the entire temperature range from 2–290 K. In the MBL samples, a nonlinear Hall response becomes evident as the temperature is raised above 150 K; hence the parallel conduction is thermally activated. In this elevated temperature regime, we now consider the additional conduction in the $\text{Al}_{0.15}\text{In}_{0.85}\text{Sb}$ buffer layer and analyze our data using a three-carrier model accordingly. As before, we fit Eq. (2b) to ρ_{xy} with the constraint that the sum of the three conductivities σ_{QW} , σ_δ , and σ_{buffer} equal the experimental value of $1/\rho_0$, where the subscript buffer refers to the buffer layer. In Fig. 5, we show the field dependence of $d\rho_{xy}/dB \equiv R_H(B)$ for the four samples at 290 K (indicated by the symbols). A smooth transition from low-field to high-field regions of constant R_H is observed in each sample, in agreement with the predictions of the multi-carrier model (see Sec. II A). The solid lines represent the least squares fits of Eq. (2b) to ρ_{xy} using three carriers. Note that in this temperature range, n_{QW} cannot be determined independently and was included as a fitting parameter. Excellent agreement with the experimental data is found for each sample over the entire field range, giving confidence in the validity of the model. Acceptable fits to ρ_{xy} could also be made with a two-carrier model; however, close inspection of $d\rho_{xy}/dB$ reveals that the model fails to fully capture the field dependence of ρ_{xy} in our samples at elevated temperatures. For completeness, these fits using the two-carrier model are shown for SBL-2 and MBL-2 in Fig. 5 by the dashed lines. It should also be noted that successful fits to ρ_{xx} using the two- or three-carrier models could not be made. Within the experimental field range, a nonsaturating MR is observed due to the presence of a positive quasilinear MR component, as inferred from the residual MR. Further discussion of this effect is beyond the scope of this paper.

The temperature dependence of the sheet density and mobility of the three layers is shown in Fig. 6. In all cases, a single high-mobility layer is found, along with two low-mobility layers. The high-mobility layer ($\approx 4 \text{ m}^2/\text{Vs}$ at 290 K)

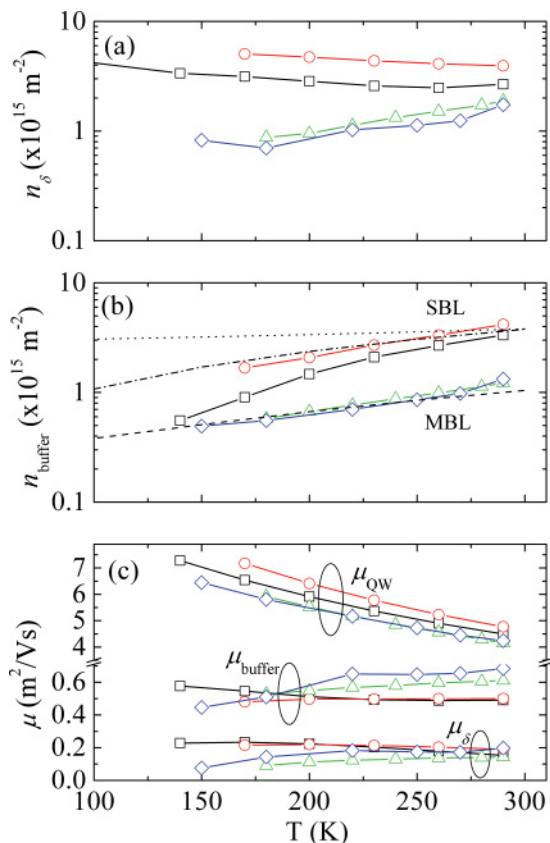


FIG. 6. (Color online) Temperature dependence of parameters determined from fits of Eq. (2a) with three carriers to ρ_{xy} of the samples (symbols); SBL-1 (\square), SBL-2 (\circ), MBL-1 (\triangle), MBL-2 (\diamond). (a) The sheet density in the $\text{Al}_{0.2}\text{In}_{0.8}\text{Sb}$ δ layer (n_δ). (b) The sheet density in the $\text{Al}_{0.15}\text{In}_{0.85}\text{Sb}$ buffer layer (n_{buffer}). (c) The electron mobility of the three layers, as indicated by the grouped data sets. The dashed and dotted lines in (b) represent the calculated sheet density for a 300-nm buffer layer appropriate for MBL samples, and a 3- μm buffer layer appropriate for SBL samples, respectively. The dot-dashed line shows the resulting sheet density when the buffer layer thickness is reduced systematically from 3 μm with decreasing temperature.

is assumed to be the InSb 2DEG. The two low-mobility layers can be distinguished by the expected temperature dependence of the sheet density, e.g. an activated temperature dependence in the buffer layer (n_{buffer}) is expected for all samples, whereas the temperature dependence of n_δ in the δ -doped $\text{Al}_{0.2}\text{In}_{0.8}\text{Sb}$ layer will be determined by the low-temperature properties of each individual sample. This distinction is clear for the SBL samples in which the $\text{Al}_{0.2}\text{In}_{0.8}\text{Sb}$ layer is occupied over the entire temperature range. In these samples at 290 K, we find $\mu_\delta \approx 0.2 \text{ m}^2/\text{Vs}$ and $\mu_{\text{buffer}} \approx 0.6 \text{ m}^2/\text{Vs}$. For

the MBL samples, the sheet density in both low-mobility channels exhibit an activated temperature dependence (since both channels are depleted at low temperatures). However, the extracted mobilities of the two layers are distinct, and their similarity to the values obtained in the SBL samples enables us to identify them. This is demonstrated by the grouped data sets in Fig. 6(c). The transport properties of each sample at 290 K are listed in Table I.

The sheet density of the buffer layer is of particular importance as this gives an indication of the expected volume-enhanced leakage in shallow etched mesoscopic devices. The MBL samples show a marked reduction in n_{buffer} compared to the SBL samples [see Fig. 6(b)]. This is compelling evidence that the $\text{Al}_{0.3}\text{In}_{0.7}\text{Sb}$ barrier layer has reduced the influence of the buffer layer on sample conduction as intended. Furthermore, the 2DEG mobility is not compromised as a result. The impact of this reduction is discussed further in Sec. IV.

At 290 K, the difference in n_{buffer} between the two sets of samples is approximately a factor of four. To understand these results, we have calculated the sheet density of the buffer layers in each sample using self-consistent solutions to the Poisson and Boltzmann equations for the conduction and valence bands of the structure.⁴⁴ In the Poisson solution, we assume a background doping density of $1 \times 10^{15} \text{ cm}^{-3}$, and midgap pinning of the Fermi level at the surface.^{24,45} The doping density in the $\text{Al}_{0.2}\text{In}_{0.8}\text{Sb}$ layer is adjusted so that the resulting QW sheet density at 10 K matches that measured from the SdH frequency. The temperature dependence of the band gaps is taken into account using the usual Varshni expression.⁴⁶ The calculated electron sheet densities in the 3- μm -thick $\text{Al}_{0.15}\text{In}_{0.85}\text{Sb}$ layer (SBL) and the isolated 300-nm $\text{Al}_{0.15}\text{In}_{0.85}\text{Sb}$ layer of the MBL samples are shown in Fig. 6(b) by the dotted and dashed lines, respectively (in the MBL, we have assumed that the upper 300-nm layer is electrically isolated from the lower 2.7- μm -thick layer and can ignore the mobile charge in the latter region owing to the height of the barrier to electron and hole transfer). Excellent agreement is found in both the temperature dependence and magnitude of n_{buffer} for the MBL samples. The calculated sheet density of the 3- μm -thick buffer layer (dotted line in Fig. 6) agrees well with the experimental data from both SBL samples at 290 K; although, in this case, the calculation fails to reproduce the temperature dependence observed experimentally. The agreement with the simulations at 290 K for both MBL and SBL samples implies that the electrically active layers are close to the anticipated thicknesses and, moreover, that the incorporation of the pseudomorphic $\text{Al}_{0.3}\text{In}_{0.7}\text{Sb}$ layer successfully isolates the underlying buffer layer from the transport measurement. The origin of the anomalous temperature dependence of n_{buffer} in the SBL samples is unclear. The fact that the calculation

TABLE I. Room temperature electronic properties for both sets of samples determined from the three-carrier model.

Sample	n_{QW} (10^{15} m^{-2})	μ_{QW} (m^2/Vs)	l_0 (nm)	n_δ (10^{15} m^{-2})	μ_δ (m^2/Vs)	n_{buffer} (10^{15} m^{-2})	μ_{buffer} (m^2/Vs)
SBL-1	6.18	4.49	583	2.67	0.15	3.33	0.49
SBL-2	6.65	4.77	643	3.93	0.19	4.17	0.50
MBL-1	7.31	4.15	586	1.88	0.14	1.22	0.61
MBL-2	6.52	4.24	566	1.74	0.19	1.32	0.68

overestimates the sheet density as the temperature is lowered may indicate a reduction in thickness of the electrically active layer. Such behavior would be consistent with the heavily dislocated regions near the AlSb-GaAs interface freezing out. Since these dislocations can propagate over $2 \mu\text{m}$ from the interface,² one may expect a potentially substantial change in properties as the temperature is lowered. We can empirically model this effect by reducing the buffer layer thickness in the Poisson model. The simulation for a structure whose buffer layer thickness reduces at a rate of 10 nm/K is shown by the dot-dashed line in Fig. 6(b) and bears some resemblance to the observed trend. We emphasize that this effect is not substantiated; however, this simple picture does provide insight to the electrical behavior of the buffer layer.

IV. DISCUSSION

To assess the impact of the reduced buffer layer conduction found in the MBL samples on mesoscopic devices, we calculate the conductance of the 2DEG and the underlying buffer layer for a realistic device geometry defined by shallow mesa etching. The geometry considered is shown schematically in the inset to Fig. 7. For simplicity, we consider a four-terminal symmetric cross junction with leads constructed of a wide region (W) and a narrow region (w) of length l and l' , respectively, on top of a square sheet of buffer layer. If we assume that the buffer layer leakage current is not confined to the mesa sidewalls and may extend laterally over the whole

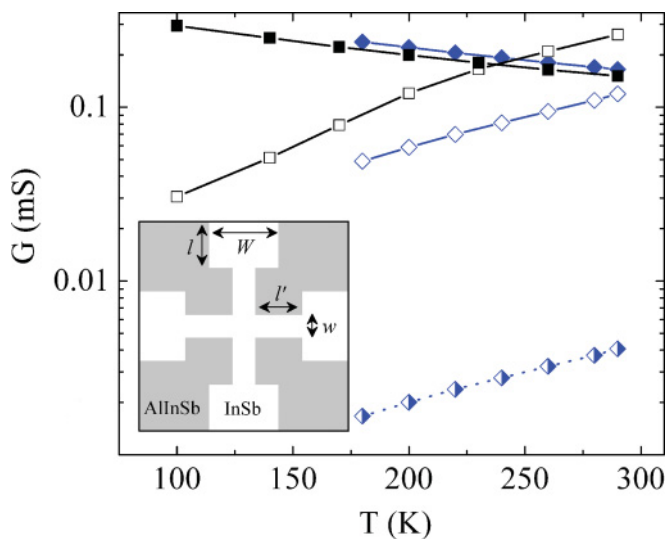


FIG. 7. (Color online) Calculated conductance G of a 2DEG patterned by shallow mesa-etching ($G_{2\text{DEG}}$, solid symbols) and an underlying sheet of buffer layer (G_{buffer} , open symbols) for an SBL (squares) and MBL (diamonds) sample using experimental conductivities obtained from the previous section. Inset shows the geometry of the device and relevant dimensions used in the calculations. A crossover occurs in the SBL sample at intermediate temperatures when $G_{\text{buffer}} \sim G_{2\text{DEG}}$, responsible for the observed decay of ballistic anomalies reported in Ref. 15. The half-filled diamonds show the calculated G_{buffer} of an MBL sample for the ideal case of when the buffer layer conduction is laterally confined to the mesa sidewalls (i.e. when the barrier layer is removed by the etch).

sheet, the two-terminal conductance of the 2DEG and buffer layer is then approximately $G_{2\text{DEG}} \approx \sigma_{\text{QW}}(2l/W + 2l'/w)^{-1}$ and $G_{\text{buffer}} \approx \sigma_{\text{buffer}}$, respectively, where σ_{QW} and σ_{buffer} are the sheet conductivities determined in the previous section (for the purpose of this calculation, σ_{QW} is assumed independent of w). This assumption is valid in both heterostructures for etch depths less than 300 nm and represents the upper limit of G_{buffer} . We consider a 250-nm -wide cross with $l'/w \sim 8$ and $l/W \sim 6.6$, which is equivalent to devices recently studied in Ref. 16. The results of $G_{2\text{DEG}}$ and G_{buffer} for the SBL-1 and MBL-1 samples are shown in Fig 7. In the SBL sample, we see the striking result that a crossover occurs, after which the conductance of the buffer layer sheet exceeds that of the patterned 2DEG. In this case, the crossover occurs at approximately 230 K , which is close to the temperatures at which ballistic transport anomalies are observed to vanish in InSb QWs.^{11,15} We interpret this as the temperature when ballistic anomalies cease to be resolved. By contrast, no crossover occurs for the MBL sample in the range of temperatures studied.

For etch depths such that the $\text{Al}_{0.3}\text{In}_{0.7}\text{Sb}$ layer is removed, one can consider the buffer layer conduction to be laterally confined to the mesa and G_{buffer} is reduced by the same geometrical factor as for the 2DEG. This ideal case is shown by the half-filled diamonds and is equivalent to that achieved in lattice matched AlGaAs/InGaAs structures⁴⁷ that are sufficiently thin to permit full mesa isolation. Now $G_{2\text{DEG}}$ exceeds G_{buffer} by over an order of magnitude at 290 K . Therefore, by extrapolation, we can infer that ballistic transport in a patterned device will still be observed at room temperature, provided the critical device dimensions (in this case w) are less than l_0 . Table I lists the values of l_0 at 290 K for the samples studied. In all cases, $l_0 \sim 600 \text{ nm}$.

We note that the mean free path deduced from the electron mobility and density represents the average path length after which an electron scatters sufficient times to lose all its momentum in a given direction. This may involve a number of small-angle scattering events or a single large-angle scattering event. As discussed by Spector *et al.*,⁴⁸ in mesoscopic structures involving large injector-collector separations, small-angle scattering events may be sufficient to alter the electron trajectory and, hence, the transmission probability. This process is characterized by a decay length typically less than l_0 .⁴⁸ The case of high-temperature ballistic transport is interesting then as electron-phonon scattering is the dominant source of momentum scattering, which is typically characterized by an isotropic scattering angle distribution. It is therefore quite reasonable that for sizable ballistic anomalies to be observed at RT, one may require l_0 to greatly exceed the critical device dimensions. A detailed understanding of just how scattering angles play a role in ballistic anomalies has not been established and would be of interest, particularly in light of experiments^{11,49} which propose to utilize such anomalies for RT applications.

V. SUMMARY

InSb/ $\text{Al}_x\text{In}_{1-x}\text{Sb}$ QW heterostructures display inherent parallel conduction in the buffer layer that significantly impedes the study, at room temperature, of nanoscale devices defined by shallow mesa etching. A comparative magnetotransport study

of two types of InSb/Al_xIn_{1-x}Sb QW heterostructures, with and without a thin pseudomorphic Al_yIn_{1-y}Sb ($y > x$) barrier layer below the QW, was presented. A multicarrier transport model was used to understand the total current through the devices in the doped Al_{0.2}In_{0.8}Sb top cap, InSb 2DEG, and Al_{0.15}In_{0.85}Sb buffer layer. The model successfully captures the Hall resistance over the entire experimental field range, enabling the determination of respective conductivities. In particular, we have demonstrated that the incorporation of a wide-band-gap barrier layer beneath the QW can significantly reduce the influence of parallel conduction in this region

for nanostructured devices without the need for improved metamorphic buffer layer technology. The resulting material has the potential to exhibit ballistic transport behavior up to room temperature without the need for an impractical deep isolation etch.

ACKNOWLEDGMENTS

The authors wish to thank J. J. Harris for useful discussions during the course of this work. This work was supported by the UK EPSRC under Grant No. EP/F065922/1.

- ¹T. Ashley, L. Buckle, S. Datta, M. T. Emeny, D. G. Hayes, K. P. Hilton, R. Jefferies, T. Martin, T. J. Phillips, D. J. Wallis, P. J. Wilding, and R. Chau, *Electron. Lett.* **43**, 777 (2007).
- ²M. Radosavljevic, T. Ashley, A. Andreev, S. D. Coomber, G. Dewey, M. T. Emeny, M. Fearn, D. G. Hayes, K. P. Hilton, M. K. Hudait, R. Jefferies, T. Martin, R. Pillarisetty, W. Rachmady, T. Rakshit, S. J. Smith, M. J. Uren, D. J. Wallis, P. J. Wilding, R. Chau, in *Electron Devices Meeting, 2008. IEDM 2008*. (IEEE International, 2008), p. 1.
- ³B. R. Bennett, R. Magno, J. B. Boos, W. Kruppa, and M. G. Ancona, *Solid-State Electron.* **49**, 1875 (2005).
- ⁴T. D. Boone, N. Smith, L. Folks, J. A. Katine, E. E. Marinero, and B. A. Gurney, *IEEE Electron Device Lett.* **30**, 117 (2009).
- ⁵S. A. Solin, D. R. Hines, A. C. H. Rowe, J. S. Tsai, Y. A. Pashkin, S. J. Chung, N. Goel, and M. B. Santos, *Appl. Phys. Lett.* **80**, 4012 (2002).
- ⁶O. Kazakova, V. Panchal, J. Gallop, P. See, D. C. Cox, M. Spasova, and L. F. Cohen, *J. Appl. Phys.* **107**, 09E708 (2010).
- ⁷K. J. Goldammer, W. K. Liu, G. A. Khodaparast, S. C. Lindstrom, and M. B. Johnson, *J. Vac. Sci. Technol. B* **16**, 1367 (1998).
- ⁸J. M. S. Orr, A. M. Gilbertson, M. Fearn, O. W. Croad, C. J. Storey, L. Buckle, M. T. Emeny, P. D. Buckle, and T. Ashley, *Phys. Rev. B* **77**, 165334 (2008).
- ⁹A. M. Gilbertson, W. R. Branford, M. Fearn, L. Buckle, P. D. Buckle, T. Ashley, and L. F. Cohen, *Phys. Rev. B* **79**, 235333 (2009).
- ¹⁰M. Hara, J. Shibata, T. Kimura, and Y. Otani, *Appl. Phys. Lett.* **88**, 082501 (2006).
- ¹¹A. M. Gilbertson, D. Benstock, M. Fearn, A. Kormányos, S. Ladak, M. T. Emeny, C. J. Lambert, T. Ashley, S. A. Solin, L. F. Cohen, *Appl. Phys. Lett.* **98**, 062106 (2011).
- ¹²A. M. Song, A. Lorke, A. Kriele, J. P. Kotthaus, W. Wegscheider, and M. Bichler, *Phys. Rev. Lett.* **80**, 3831 (1998).
- ¹³Y. V. Pershin and C. Piermarocchi, *Phys. Rev. B* **72**, 195340 (2005).
- ¹⁴S. Sassine, Y. Krupko, J. C. Portal, Z. D. Kvon, R. Murali, K. P. Martin, G. Hill, and A. D. Wieck, *Phys. Rev. B* **78**, 045431 (2008).
- ¹⁵N. Goel, S. J. Chung, M. B. Santos, K. Suzuki, S. Miyashita, and Y. Hirayama, *Physica E-Low-Dimensional Systems & Nanostructures* **20**, 251 (2004).
- ¹⁶A. M. Gilbertson, M. Fearn, A. Kormányos, D. E. Read, C. J. Lambert, M. T. Emeny, T. Ashley, S. A. Solin, and L. F. Cohen, *Phys. Rev. B* **83**, 075304 (2011).
- ¹⁷J. M. S. Orr, P. D. Buckle, M. Fearn, C. J. Bartlett, L. Buckle, and T. Ashley, *AIP Conf. Proc.* **893**, 729 (2007).
- ¹⁸J. M. S. Orr, P. D. Buckle, M. Fearn, C. J. Storey, L. Buckle, and T. Ashley, *New J. Phys.* **9**, 261 (2007).
- ¹⁹T. Zhang, S. K. Clowes, M. Debnath, A. Bennett, C. Roberts, J. J. Harris, R. A. Stradling, L. F. Cohen, T. Lyford, and P. F. Fewster, *Appl. Phys. Lett.* **84**, 4463 (2004).
- ²⁰T. Zhang, J. J. Harris, W. R. Branford, S. K. Clowes, L. F. Cohen, and S. A. Solin, *Semicond. Sci. Technol.* **21**, 1543 (2006).
- ²¹O. J. Pooley, A. M. Gilbertson, P. D. Buckle, R. S. Hall, L. Buckle, M. T. Emeny, M. Fearn, L. F. Cohen, and T. Ashley, *New J. Phys.* **12**, 053022 (2010).
- ²²K. J. Goldammer, S. J. Chung, W. K. Liu, M. B. Santos, J. L. Hicks, S. Raymond, and S. Q. Murphy, *J. Cryst. Growth* **201–202**, 753 (1999).
- ²³N. Dai, G. A. Khodaparast, F. Brown, R. E. Doezema, S. J. Chung, and M. B. Santos, *Appl. Phys. Lett.* **76**, 3905 (2000).
- ²⁴J. M. S. Orr, P. D. Buckle, M. Fearn, P. J. Wilding, C. J. Bartlett, M. T. Emeny, L. Buckle, and T. Ashley, *Semicond. Sci. Technol.* **21**, 1408 (2006).
- ²⁵D. A. Syphers, K. P. Martin, and R. J. Higgins, *Appl. Phys. Lett.* **49**, 534 (1986).
- ²⁶M. J. Kane, N. Apsley, D. A. Anderson, L. L. Taylor, and T. Kerr, *J. Phys. C: Solid State Physics* **18**, 5629 (1985).
- ²⁷U. Zeitler and A. G. M. Jansen, *Physica B: Condensed Matter* **204**, 90 (1995).
- ²⁸V. K. Arora and M. Jaafarian, *Phys. Rev. B* **13**, 4457 (1976).
- ²⁹A. A. Abrikosov, *Europhys. Lett.* **49**, 789 (2000).
- ³⁰T. Zhang, J. J. Harris, W. R. Branford, Y. V. Bugoslavsky, S. K. Clowes, L. F. Cohen, A. Husmann, and S. A. Solin, *Appl. Phys. Lett.* **88**, 012110 (2006).
- ³¹P. T. Coleridge, A. S. Sachrajda, and P. Zawadzki, *Phys. Rev. B* **65**, 125328 (2002).
- ³²J. Hu and T. F. Rosenbaum, *Nat. Mater.* **7**, 697 (2008).
- ³³A. L. Friedman, J. L. Tedesco, P. M. Campbell, J. C. Culbertson, E. Aifer, F. K. Perkins, R. L. Myers-Ward, J. K. Hite, C. R. Eddy Jr., G. G. Jernigan, D. K. Gaskill, *Nano Lett.* **10**, 3962 (2010).
- ³⁴G. Bergmann, *Phys. Rep.-Rev. Sec. Phys. Lett.* **107**, 1 (1984).
- ³⁵P. A. Lee and T. V. Ramakrishnan, *Rev. Mod. Phys.* **57**, 287 (1985).
- ³⁶B. L. Altshuler, A. G. Aronov, and P. A. Lee, *Phys. Rev. Lett.* **44**, 1288 (1980).
- ³⁷E. Abrahams, S. V. Kravchenko, and M. P. Sarachik, *Rev. Mod. Phys.* **73**, 251 (2001).
- ³⁸A. M. Gilbertson, A. K. M. Newaz, W. J. Chang, R. Bashir, S. A. Solin, and L. F. Cohen, *Appl. Phys. Lett.* **95**, 012113 (2009).

- ³⁹S. A. Studenikin, P. T. Coleridge, N. Ahmed, P. J. Poole, and A. Sachrajda, *Phys. Rev. B* **68**, 035317 (2003).
- ⁴⁰J. J. Lin and J. P. Bird, *J. Phys. Condens. Matter* **14**, R501 (2002).
- ⁴¹B. L. Altshuler, A. G. Aronov, and D. E. Khmel'nitsky, *J. Phys. C-Solid State Physics* **15**, 7367 (1982).
- ⁴²J. M. S. Orr, A. M. Gilbertson, M. Fearn, O. W. Croad, C. J. Storey, L. Buckle, M. T. Emeny, P. D. Buckle, and T. Ashley, *Phys. Rev.* **77**, 165334 (2008).
- ⁴³O. J. Pooley, A. M. Gilbertson, P. D. Buckle, R. S. Hall, M. T. Emeny, M. Fearn, M. P. Halsall, L. F. Cohen, T. Ashley, *Semi. Sci. Tech.* **25**, 125005 (2010).
- ⁴⁴I. H. Tan, G. L. Snider, L. D. Chang, and E. L. Hu, *J. Appl. Phys.* **68**, 4071 (1990).
- ⁴⁵A. M. Gilbertson, J. M. S. Orr, P. D. Buckle, S. Clowes, M. Fearn, C. J. Storey, L. Buckle, L. F. Cohen, and T. Ashley, *Phys. Rev. B* **76**, 085306 (2007).
- ⁴⁶N. Dai, F. Brown, R. E. Doezema, S. J. Chung, K. J. Goldammer, and M. B. Santos, *Appl. Phys. Lett.* **73**, 3132 (1998).
- ⁴⁷Y. Hirayama and S. Tarucha, *Appl. Phys. Lett.* **63**, 2366 (1993).
- ⁴⁸J. Spector, H. L. Stormer, K. W. Baldwin, L. N. Pfeiffer, and K. W. West, *Surf. Sci.* **228**, 283 (1990).
- ⁴⁹A. M. Song, P. Omling, L. Samuelson, W. Seifert, I. Shorubalko, and H. Zirath, *Appl. Phys. Lett.* **79**, 1357 (2001).